



<https://doi.org/10.11646/mesozoic.1.3.12>

<http://zoobank.org/urn:lsid:zoobank.org:pub:0CBF57A1-8D36-4006-9241-748F622FE4CB>

## Late Cretaceous rapid exhumation of the Central Tibetan Plateau: Insights from low-temperature thermochronology

SI-QI LI<sup>1</sup>, GAO-YUAN SUN<sup>1</sup>\*, TIAN-NAN YOU<sup>1</sup> & XIU-MIAN HU<sup>2</sup>

<sup>1</sup>College of Oceanography, Hohai University, Nanjing 210024, China

<sup>2</sup>School of Earth Science and Engineering, Nanjing University, Nanjing 210023, China

✉ [lisiqi0320@126.com](mailto:lisiqi0320@126.com); <https://orcid.org/0009-0006-5985-5013>

✉ [sungy@hhu.edu.cn](mailto:sungy@hhu.edu.cn); <https://orcid.org/0000-0002-0914-0398>

✉ [1848356446@qq.com](mailto:1848356446@qq.com); <https://orcid.org/0009-0005-6084-7638>

✉ [huxm@nju.edu.cn](mailto:huxm@nju.edu.cn); <https://orcid.org/0000-0002-5401-8682>

\*Corresponding author

### Abstract

The uplift history of the Tibetan Plateau is a hot topic for the geological study. The Lhasa terrane, situated on the southern edge of Eurasian plate, records the tectonic evolution of the Tibetan Plateau preceding the collision between the Indian and Eurasian continental plates. This paper employs low-temperature thermochronological methods, including zircon and apatite (U-Th)/He dating, as well as apatite fission track (AFT) analysis, to investigate the Bange pluton in the northern Lhasa terrane. The research results indicate that the zircon and apatite helium (ZHe and AHe) ages from the plutons range from 90 to 78 Ma and 83 to 63 Ma, respectively, while the AFT ages span from 65 to 46 Ma. Thermal history reveals that the Bange pluton experienced a rapid cooling phase during the Late Cretaceous (from ~94 to 70 Ma), with a cooling rate of ~4.2 °C/Ma, subsequently followed by a slow cooling rate with ~1.1 °C/Ma. These results suggest that the Bange pluton has undergone rapid uplift during the Late Cretaceous to Paleocene. This Late Cretaceous rapid cooling event is also observed in other regions of the Lhasa terrane, indicating a widespread period of rapid cooling and exhumation. Since the Cenozoic, the cooling rate of the Bange pluton has significantly decreased, which would suggest that the tectonic uplift of the central Tibetan Plateau may not be related to the India-Asia continental collision. Considering the regional tectonic context, the collision between the Lhasa terrane and the Qiangtang terrane during the Late Jurassic to Early Cretaceous may have initiated the exhumation of the Lhasa terrane in the Late Cretaceous.

**Keywords:** Bange pluton, low-temperature thermochronology, Tibetan Plateau, uplift history

### Introduction

The Tibetan Plateau orogenic belt, formed by the collision and convergence of a series of the continents (such as the collisions of Lhasa and Qiangtang terranes, Indian and Eurasian plates), is one of the largest orogenic belts on the Earth (Wu *et al.*, 2008; Hetzel, 2013; Ding *et al.*, 2022). Its tectonic and uplift history holds significant implications for studying geodynamics and global climate change (Shi *et al.*, 1999; Wang *et al.*, 2014; He *et al.*, 2022). The Lhasa terrane is situated within the interior of the Tibetan Plateau orogenic belt, structurally positioned along the southern margin of the Asian continent, documenting the uplift evolution history of the plateau (Wang *et al.*, 2014). However, there remains controversy over whether early uplift of the Tibetan Plateau existed prior to the India-Eurasia collision (Pan *et al.*, 2006; Dai *et al.*, 2013; Hu *et al.*, 2020; Qian *et al.*, 2021).

Under the effects of the Lhasa-Qiangtang collision and the subduction of the Neotethys plate, the Lhasa terrane underwent significant deformation and crustal shortening during the Late Jurassic-Cretaceous, thus forming the initial tectonic uplift on the surface (Murphy *et al.*, 1997; Kapp *et al.*, 2007; Zhang *et al.*, 2014; Li *et al.*, 2015). The crustal shortening and thickening within the plateau in the Late Cretaceous are also supported by petrological and sedimentological evidence (Ding & Lai, 2003; Sun *et al.*, 2015a, b; Lai *et al.*, 2019). Other studies have suggested that the Lhasa terrane collided with the Qiangtang terrane and rose rapidly in the Cretaceous, followed by a topographical reconfiguration caused by the collapse of the orogenic belt in the Paleocene, forming

the “Central Valley of the Plateau” (Ding *et al.*, 2022). The final uplift of the plateau to its current height would occur after the Eocene-Oligocene (Hu *et al.*, 2020; Xiong *et al.*, 2022).

Low-temperature thermochronology is a valuable method for detecting rock exhumation. Numerous low-temperature thermochronological data have been published for the Lhasa terrane (Fig. 1A). Rohrmann *et al.*, (2012) conducted low-temperature thermochronology analyses within the plateau interior and suggested that the rapid exhumation during the Late Cretaceous to Middle Eocene period (85–45 Ma), yielded the initial growth on the plateau. Subsequently, after 45 Ma, the exhumation rate notably decelerated, indicating a low-relief topography in central Tibet. In contrast, Hetzel *et al.* (2011) proposed that the exhumation process from the Late Cretaceous to Eocene was characterized by peneplanation. Until approximately 50 Ma, the plateau remained at an elevation close to the sea level. Low-temperature data obtained from the Gaize area of the western Bangong-Nujiang suture zone reveal a three-stage cooling history: 120–100 Ma, 85–55 Ma, and 47–30 Ma (Li *et al.*, 2022; Tong *et al.*, 2022). These cooling events were influenced by the crustal deformation and shortening resulting from the Lhasa-Qiangtang collision, northward subduction of the Neo-Tethys oceanic crust, and the India-Asia continental collision. Despite the substantial low-temperature thermochronological dataset available from the Tibetan Plateau, ongoing debates existed regarding the interpretation of these findings, including differing perspectives on the timing of the uplift on the plateau.

The Bange area is located in the northern part of the Lhasa terrane and featured as the peneplain. It has experienced crustal shortening caused by the collision between the Lhasa and Qiangtang terranes (Hetzel *et al.*, 2011). The Bange region is dominated by low-relief landscape, with basically no sediments after the Eocene (Strobl *et al.*, 2010), which is a proper object to study the early uplift process of the plateau before the India-Asia collision.

For this study, we investigated the Bange pluton located in the northern part of the Lhasa terrane and employed a combination of ZHe, AHe and AFT analysis, to reconstruct the thermal evolution history of the pluton. Through a comparative analysis of published data and integration with regional geological information, the study reveals that the uplift of the Lhasa terrane has occurred since the Late Cretaceous, predated to the India-Asia continental collision. The collision between the Lhasa and Qiangtang terrane during the Late Jurassic and Early Cretaceous would perform as a plausible contribution for this tectonic uplift.

## Geological setting

The Lhasa terrane is situated in the central region of the Tibetan Plateau, spanning approximately 2000 km from east to west. It is bordered by the Qiangtang terrane to the north and the Himalaya terrane to the south. This terrane lies between the Indus-Yarlung suture zone and the Bangong-Nujiang suture zone, extending in an east-west direction (Kapp & Decelles, 2019) (Fig. 1A). The Lhasa terrane can be subdivided into three subterrane from south to north: the South Lhasa subterrane; the Central Lhasa subterrane; and the North Lhasa subterrane, which are separated by the Luobadui-Milashan fault and the Shiquanhe-Nam Co ophiolite mélange zone (Zhu *et al.*, 2013). The North Lhasa subterrane primarily comprises Mesozoic volcanoclastic and sedimentary rock strata along with corresponding intrusive rocks. The Precambrian crystalline basement is exposed in the Anduo area (Zhu *et al.*, 2011). The Central Lhasa subterrane includes Paleozoic-Mesozoic sedimentary rocks, volcanic rocks, and associated intrusive rocks. In the Shenzha area, some Paleozoic strata are exposed (Zhu *et al.*, 2009). Some studies have revealed that the Central Lhasa subterrane contains significant Precambrian metamorphic basement (Zhu *et al.*, 2011), as well as Palaeogene granitic gneiss exposed in the Nyenchenthanglha Group (Hu *et al.*, 2005). The South Lhasa subterrane is characterized by the Gangdese Batholith, which includes rock assemblages from various periods, such as Cretaceous-Palaeogene intrusive plutons, Paleocene-Eocene Linzizong volcanic rocks, and Jurassic-Cretaceous sedimentary strata (Zhu *et al.*, 2009).

The Bange pluton of this study is situated in the North Lhasa subterrane, near the Shiquanhe-Nam Co ophiolite mélange and the Central Lhasa subterrane to the southwest (Fig. 1B). The Cenozoic volcanic-sedimentary strata and Mesozoic igneous rocks are exposed, including the Yongzhu, Danlin, Chaguoloma, Shilangmusi, Duoni, Langshan, Jingzhushan, and Niubao formations. The Yongzhu Formation consists of Carboniferous granites, with the overlying Danlin and Chaguoloma formations. The Cretaceous Duoni, Langshan and Jingzhushan formations are well exposed, with the deltaic sandstone-mudstone, Marine limestone to terrestrial conglomerates. The Jingzhushan Formation lies angular unconformable above the Langshan Formation (Lai *et al.*, 2019). Since the deposition of the Late Cretaceous Jingzhushan Formation, a ~50 Ma depositional gap (from 90–40 Ma) has occurred (Sun *et al.*, 2024), with followed by the Eocene Niubao Formation. The ~90 Ma magmatic rocks are widespread among the northern Lhasa terrane. The Bange area is extensively exposed by the Cretaceous to Palaeogene magmatic rocks, and Quaternary sediments. The samples

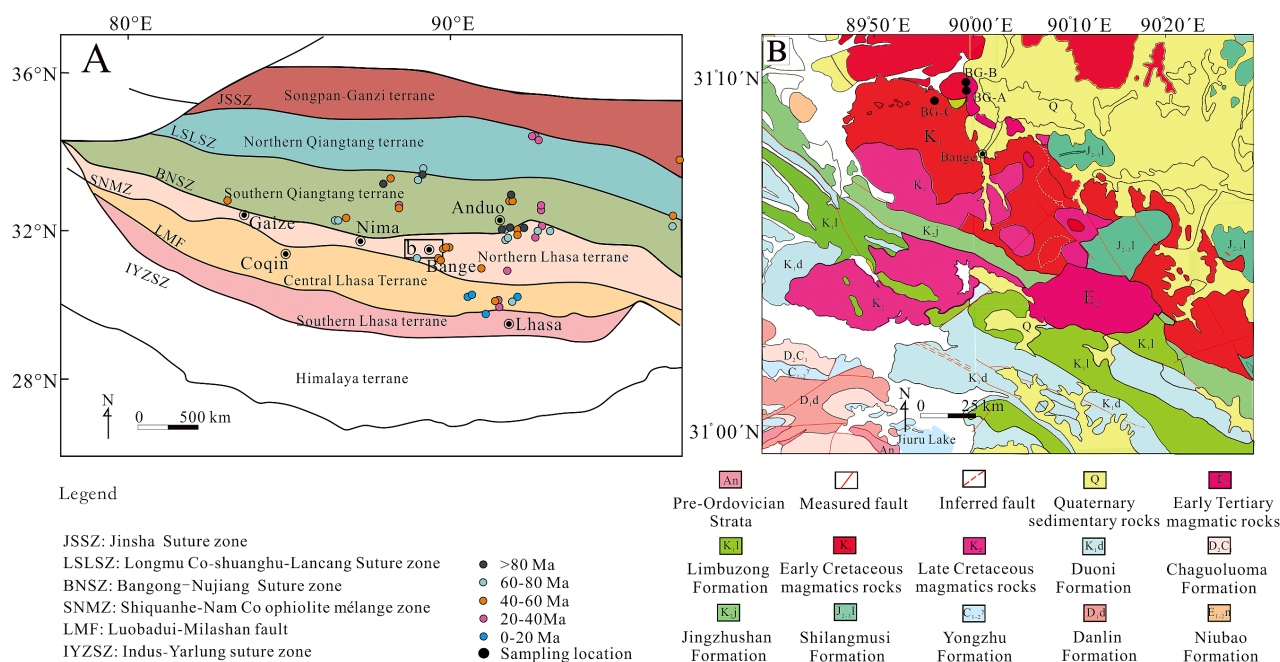


**FIGURE 1.** Simplified geological map of Tibetan Plateau and study area. **A**, Structural map of the Tibetan Plateau and compilation of the time of rapid uplift of the Lhasa terrane, showing the main tectonic zones of the Qinghai-Tibet Plateau, modified from Zhang *et al.*, (2022), mainly referring to published low-temperature thermochronological data. (Wang *et al.*, 2007; Hetzel *et al.*, 2011; Dai *et al.*, 2013, 2020; Haider *et al.*, 2013; Wang & Wei, 2013; Li, G *et al.*, 2015, 2018; Lu *et al.*, 2015; Staisch *et al.*, 2016; Li, H. *et al.*, 2019; Bi *et al.*, 2020; Yang *et al.*, 2020; Zhao *et al.*, 2020; Qian *et al.*, 2021). **B**, Geological map of the Bange area, with sample locations marked in the figure.

of this study, collected in the Bange area, are all granites and belong to the Cretaceous intrusive plutons.

## Material and methods

Three granite samples were collected from the Bange pluton (Fig. 1B). The detailed sample locations are listed in Table 1.

The samples were processed using conventional techniques, including crushing, screening, magnetic separation, and heavy liquid separation to isolate zircon and apatite. Individual zircon and apatite particles were manually selected under a microscope based on size, clarity, color, and degree of euhedral form. The U-Th/He dating for this study was carried out at the Scottish Environment University Research Centre, and the apatite fission track testing was carried out at the Low Temperature Thermochronology Laboratory, Department of Earth Sciences, University of Glasgow, Scotland.

### The apatite fission track (AFT)

The fission track analysis in this study was conducted at the Low Temperature Thermochronology Laboratory, Department of Earth Sciences, University of Glasgow,

Scotland. The samples underwent cleaning, crushing, washing, drying, and magnetic separation. Apatite crystals were then separated using tetrabromoethane and diiodomethane. The sorted apatite crystals were embedded in epoxy resin and cured at 70 °C for 24 hours. The cured samples were grounded, polished, and etched with 1% nitric acid at room temperature (25 °C) for about 20 seconds to ensure that the spontaneous tracks can be fully displayed. After completion, the samples were rinsed with clean water and fully soaked to fully remove the nitric acid.

The fission track ages were determined using the external detector method, with a Zeta value of 320 ± 20 obtained in this laboratory. The etched samples were securely attached to low-uranium muscovite sheets and labeled to distinguish between spontaneous and induced tracks. The samples, along with standard uranium glass IRMM and age standards Durango and Fish Canyon Tuff, were conducted for irradiation. Then, the samples were etched with hydrofluoric acid at room temperature (25 °C) for about 1 hour to fully reveal the induced tracks. Finally, the apatite particles and muscovite sheets were mounted on a glass plate in a mirror-image configuration, and the density and length of the spontaneous and induced tracks were measured using a high-power microscope.

### Zircon U-Pb dating

The zircons in the samples were crushed, magnetically screened and separated by heavy liquid, and then observed under a binocular microscope to select zircon particles with good automorphism, that is, no inclusions and obvious cracks. The selected zircon grains were then polished with epoxy resin to expose the crystal centers. Zircon U-Pb isotope analysis was conducted at the State Key Laboratory of Mineral Deposits Research, Nanjing University, using laser ablation inductively coupled plasma mass spectrometry (LA-ICP-MS). Elemental and isotopic ion signal intensities were measured with an Agilent 213a ICP-MS. Before analysis, the ablated material was transported by helium carrier gas through a PVC tube with a 30 mm inner diameter and embedded in a 30 cm<sup>3</sup> capacity cube. The analysis was repeated using a laser beam with a diameter of 30 μm and a frequency of 5 Hz, each time lasting about 100 seconds, and the raw count rates of <sup>206</sup>Pb, <sup>207</sup>Pb, <sup>208</sup>Pb, <sup>232</sup>Th and <sup>238</sup>U were collected for age determination. Mass spectrometer calibration and correction for elemental fractionation were performed using homogeneous zircon standards, as detailed by Jackson *et al.* (2004). The raw U-Pb isotope data from ICP-MS were exported in ASCII format and processed using GLITTER4.4 software. For zircons younger than 1000 Ma, <sup>206</sup>Pb/<sup>238</sup>U ages were used; for zircons older than 1000 Ma, <sup>207</sup>Pb/<sup>206</sup>Pb ages were used.

#### Zircon (U-Th)/He (ZHe)

Zircon grains with good euhedral form, no inclusions or obvious cracks, and appropriate size and roundness were selected from the pre-sorted zircon particles. The zircon crystals were chosen to be smaller than 70 μm in diameter to prevent incomplete dissolution of overly large particles and to avoid the excessive correction factors associated with very small particles, which can affect experimental results. The selected zircon crystals were examined under a binocular microscope to measure their length, width, and height. Based on the distance of α-particle migration within the zircon particles and U-Th analysis, the Th/U ratio was determined, providing the α-particle correction parameter Ft (Reiners, 2005). The extraction and analysis of <sup>4</sup>He were performed using a quadrupole mass spectrometer, with each step repeated at least twice to ensure complete extraction and analysis. Subsequently, a purification process lasting approximately 2 minutes

was conducted using the mass spectrometer to thoroughly purify the <sup>4</sup>He. The purified <sup>4</sup>He was then mixed with a known quantity of <sup>3</sup>He to calculate the <sup>4</sup>He content.

#### Apatite (U-Th)/He (AHe)

Among the selected apatite particles, those with good euhedral form, no inclusions, and no obvious cracks, and a suitable size (preferably 50–70 μm to retain as much <sup>4</sup>He as possible) were chosen under orthogonal conditions using a microscope. The selected apatite particles were then placed in a glass container. For each sample, 3–5 apatite particles that met these criteria were chosen as test samples. These samples were observed and photographed under a microscope, and their length, width, and height were measured.

The apatite crystals were placed in metal foil containers and kept in a closed environment that allowed unobstructed gas exchange. A laser beam was used to heat the metal foil containers to approximately 1000 °C for about 120 seconds to fully extract <sup>4</sup>He. The extracted <sup>4</sup>He was then fully mixed with <sup>3</sup>He at a concentration of not less than 0.1 pmol in a low-temperature environment. Activated carbon was used to purify the mixed <sup>4</sup>He and <sup>3</sup>He to the greatest extent. The ratio of <sup>4</sup>He/<sup>3</sup>He was determined using a quadrupole mass spectrometer, and the concentration of <sup>4</sup>He was calculated based on this ratio. The apatite crystals with the tested <sup>4</sup>He/<sup>3</sup>He ratio were added to a concentrated nitric acid solution containing calibrated <sup>230</sup>Th and <sup>235</sup>U. The solution was shaken using an ultrasonic instrument to ensure that the apatite particles were fully dissolved. Finally, the resulting solution was placed in an ICP-MS to measure the ratios of <sup>238</sup>U/<sup>233</sup>U and <sup>232</sup>Th/<sup>229</sup>Th. The (U-Th)/He age was calculated using this data.

## Results

#### Apatite fission track

Three samples collected in this study were analyzed using apatite fission track methods, with detailed data presented in Table 1. The fission track ages were determined as follows: sample BG-A is 64.9 ± 4.4 Ma, sample BG-B is 56.0 ± 3.8 Ma, and sample BG-C is 45.7 ± 3.3 Ma. The

**TABLE 1.** Apatite fission track data of Bange pluton.

Sample	GPS		Grains	$\rho_s \times 10^5 \text{cm}^{-2}$ (Ns)	$\rho_i \times 10^5 \text{cm}^{-2}$ (Ni)	$\rho_d \times 10^5 \text{cm}^{-2}$ (Nd)	P (χ <sup>2</sup> )	Age (Ma)	Length (μm) / nubles
BG-A	31°28'39.2"N	89°49'43.4"E	20	13.9 (2296)	32.3 (5334)	9.47 (5796)	0.16	64.9 ± 4.4	14.0 ± 1.1/51
BG-B	31°28'39.2"N	89°49'43.4"E	20	11.5 (1969)	29.0 (4973)	8.89 (5441)	0.025	56.0 ± 3.8	13.9 ± 1.0/50
BG-C	31°29'10.7"N	89°55'45.0"E	20	8.02 (1095)	26.2 (3570)	9.34 (5717)	0.0012	45.7 ± 3.3	13.5 ± 1.4/50

Note:  $\rho_s$ —spontaneous track density;  $\rho_i$ —induced track density;  $\rho_d$ —standard glass track density; Zeta = 320 ± 20; Length—average track length

**TABLE 2.** Analytical results of the Sample BG-B zircon U-Pb age.

No.	Corrected ratios		Corrected ages (Ma)										Disc. (%)	Best ages						
	$^{207}\text{Pb}/^{206}\text{Pb}$	$1\sigma$	$^{207}\text{Pb}/^{235}\text{U}$	$1\sigma$	$^{206}\text{Pb}/^{238}\text{U}$	$1\sigma$	$^{207}\text{Pb}/^{238}\text{U}$	$1\sigma$	$^{208}\text{Pb}/^{232}\text{Th}$	$1\sigma$	$^{207}\text{Pb}/^{206}\text{Pb}$	$1\sigma$			$^{207}\text{Pb}/^{235}\text{U}$	$1\sigma$	$^{206}\text{Pb}/^{238}\text{U}$	$1\sigma$	$^{208}\text{Pb}/^{232}\text{Th}$	$1\sigma$
G13	0.04828	0.00138	0.12702	0.00372	0.01908	0.0003	0.0037	0.00567	0.00037	113	67	121	3	122	2	114	7	-1	122	2
G25	0.04749	0.00144	0.12618	0.00391	0.01927	0.0003	0.0038	0.00628	0.00038	74	68	121	4	123	2	127	8	-2	123	2
G11	0.05178	0.00164	0.14033	0.00452	0.01966	0.00034	0.00199	0.01381	0.00199	276	74	133	4	126	2	277	40	6	126	2
G23	0.0492	0.00173	0.13506	0.00478	0.01991	0.00033	0.0004	0.00591	0.0004	157	84	129	4	127	2	119	8	2	127	2
G06	0.05167	0.00201	0.14404	0.00554	0.02022	0.00034	0.00041	0.00613	0.00041	271	91	137	5	129	2	124	8	6	129	2
G21	0.04809	0.0019	0.13893	0.00549	0.02096	0.00035	0.00038	0.00677	0.00038	104	90	132	5	134	2	136	8	-1	134	2
G10	0.04914	0.0014	0.14411	0.00414	0.02128	0.00033	0.00131	0.01625	0.00131	155	68	137	4	136	2	326	26	1	136	2
G22	0.0487	0.0029	0.14272	0.00829	0.02126	0.00047	0.00067	0.00622	0.00067	133	135	135	7	136	3	125	13	-1	136	3
G15	0.04902	0.00147	0.14516	0.00439	0.02148	0.00033	0.00045	0.00741	0.00045	149	72	138	4	137	2	149	9	1	137	2
G17	0.04787	0.00106	0.14222	0.00338	0.02155	0.00034	0.00036	0.00632	0.00036	93	53	135	3	137	2	127	7	-1	137	2
G12	0.04899	0.00123	0.14622	0.00384	0.02165	0.00034	0.00052	0.00714	0.00052	147	60	139	3	138	2	144	10	1	138	2
G16	0.04902	0.00137	0.14673	0.00419	0.02171	0.00033	0.00038	0.00754	0.00038	149	67	139	4	138	2	152	8	1	138	2
G20	0.04887	0.00125	0.14774	0.00392	0.02193	0.00033	0.0004	0.0072	0.0004	142	61	140	3	140	2	145	8	0	140	2
G02	0.05214	0.00181	0.1615	0.00558	0.02247	0.00039	0.00258	0.02067	0.00258	292	81	152	5	143	2	414	51	6	143	2
G09	0.04832	0.00087	0.14939	0.00299	0.02242	0.00033	0.00038	0.00618	0.00038	115	43	141	3	143	2	125	8	-1	143	2
G01	0.04931	0.00092	0.15528	0.00316	0.02284	0.00033	0.00042	0.0094	0.00042	163	45	147	3	146	2	189	8	1	146	2
G08	0.05073	0.00159	0.19451	0.00617	0.02781	0.00047	0.00083	0.00987	0.00083	229	74	180	5	177	3	199	17	2	177	3
G04	0.05137	0.00158	0.23767	0.00735	0.03356	0.00054	0.00113	0.01345	0.00113	257	72	217	6	213	3	270	23	2	213	3
G26	0.05067	0.00143	0.28532	0.00823	0.04084	0.00067	0.01092	0.01092	0.01092	226	67	255	7	258	4	220	22	-1	258	4
G19	0.05157	0.00084	0.33938	0.00633	0.04774	0.0007	0.0006	0.0131	0.0006	266	38	297	5	301	4	263	12	-1	301	4
G05	0.11367	0.00308	0.80072	0.01843	0.05109	0.00073	0.00059	0.01473	0.00059	1859	50	597	10	321	4	295	12	86	321	4
G07	0.05806	0.00091	0.6419	0.01146	0.08019	0.00114	0.00122	0.02509	0.00122	532	35	503	7	497	7	501	24	1	497	7
G18	0.13263	0.00177	2.40379	0.03784	0.13148	0.00181	0.00155	0.02722	0.00155	2133	24	1244	11	796	10	543	30	56	796	10
G03	0.0676	0.00287	1.3871	0.05523	0.14882	0.00219	0.00068	0.04534	0.00068	856	90	883	23	894	12	896	13	-1	894	12
G14	0.14725	0.00171	4.07664	0.06025	0.20083	0.00277	0.00152	0.03901	0.00152	2314	20	1650	12	1180	15	773	30	40	2314	20
G24	0.10583	0.00274	3.29318	0.08926	0.22567	0.00396	0.01053	0.07773	0.01053	1729	49	1479	21	1312	21	1513	197	13	1729	49

**TABLE 3.** Analytical results of the Sample BG-C zircon U-Pb age.

NO.	Corrected ratios										Corrected ages (Ma)					Disc. (%)	Best ages		
	$^{207}\text{Pb}/^{206}\text{Pb}$	$1\sigma$	$^{207}\text{Pb}/^{235}\text{U}$	$1\sigma$	$^{206}\text{Pb}/^{238}\text{U}$	$1\sigma$	$^{206}\text{Pb}/^{232}\text{Th}$	$1\sigma$	$^{207}\text{Pb}/^{206}\text{Pb}$	$1\sigma$	$^{207}\text{Pb}/^{235}\text{U}$	$1\sigma$	$^{206}\text{Pb}/^{238}\text{U}$	$1\sigma$	$^{206}\text{Pb}/^{232}\text{Th}$			$1\sigma$	
G03	0.04873	0.00104	0.13532	0.00309	0.02014	0.00031	0.00582	0.00033	135	51	129	3	129	2	117	7	0	129	2
G09	0.04965	0.00753	0.14071	0.02049	0.02057	0.00094	0.00789	0.00266	179	305	134	18	131	6	159	53	2	131	6
G06	0.04989	0.00303	0.14484	0.00859	0.02106	0.00051	0.00731	0.00106	190	139	137	8	134	3	147	21	2	134	3
G11	0.05	0.0015	0.1462	0.00441	0.02121	0.00034	0.0064	0.0006	195	71	139	4	135	2	129	12	3	135	2
G07	0.04937	0.00172	0.14515	0.00462	0.02133	0.00031	0.00674	0.0001	165	83	138	4	136	2	136	2	1	136	2
G01	0.05004	0.0013	0.14823	0.00396	0.02149	0.00033	0.00915	0.00055	197	62	140	4	137	2	184	11	2	137	2
G22	0.0484	0.00109	0.14371	0.00341	0.02154	0.00033	0.00809	0.00045	119	54	136	3	137	2	163	9	-1	137	2
G02	0.05701	0.00169	0.16981	0.00508	0.02161	0.00036	0.00834	0.00095	492	67	159	4	138	2	168	19	15	138	2
G04	0.05417	0.003	0.16155	0.00856	0.02163	0.00035	0.00676	0.00012	378	128	152	7	138	2	136	2	10	138	2
G15	0.04919	0.00149	0.14632	0.0045	0.02157	0.00035	0.00646	0.00049	157	72	139	4	138	2	130	10	1	138	2
G23	0.04828	0.00152	0.14378	0.00462	0.0216	0.00037	0.00626	0.00056	113	73	136	4	138	2	126	11	-1	138	2
G14	0.05188	0.00303	0.15787	0.00891	0.02208	0.00049	0.01646	0.00335	280	136	149	8	141	3	330	67	6	141	3
G12	0.05002	0.00225	0.15418	0.00678	0.02236	0.00044	0.00688	0.00143	196	105	146	6	143	3	139	29	2	143	3
G10	0.05113	0.00199	0.20347	0.00776	0.02888	0.00051	0.01139	0.00182	247	92	188	7	184	3	229	36	2	184	3
G20	0.07814	0.00189	0.32569	0.00638	0.03023	0.00043	0.00906	0.00022	1150	49	286	5	192	3	182	4	49	192	3
G27	0.05627	0.00308	0.23759	0.01269	0.03062	0.00071	0.01756	0.00192	463	125	216	10	194	4	352	38	11	194	4
G05	0.05649	0.00169	0.2406	0.00632	0.03089	0.00044	0.00961	0.00016	472	68	219	5	196	3	193	3	12	196	3
G16	0.05078	0.00093	0.24056	0.00486	0.03436	0.00051	0.0112	0.00051	231	43	219	4	218	3	225	10	0	218	3
G19	0.12547	0.00157	0.68045	0.01051	0.03934	0.00056	0.00942	0.00039	2035	23	527	6	249	3	190	8	112	249	3
G21	0.05698	0.00084	0.43244	0.00742	0.05504	0.00079	0.01838	0.00089	491	33	365	5	345	5	368	18	6	345	5
G08	0.06446	0.00383	0.80271	0.04589	0.09031	0.00147	0.02766	0.00046	757	129	598	26	557	9	551	9	7	557	9
G17	0.09821	0.00134	1.59626	0.02688	0.11788	0.00177	0.03318	0.00169	1590	26	969	11	718	10	660	33	35	718	10
G25	0.15166	0.00387	2.85401	0.06025	0.13648	0.00196	0.03822	0.00064	2365	45	1370	16	825	11	758	12	66	825	11
G24	0.07591	0.00372	1.61895	0.07556	0.15467	0.00232	0.04651	0.0007	1093	101	978	29	927	13	919	14	6	927	13
G29	0.07199	0.00168	1.70757	0.04239	0.17196	0.00282	0.04839	0.00572	986	49	1011	16	1023	16	955	110	-1	986	49
G18	0.12974	0.00368	4.44838	0.10768	0.24868	0.00369	0.07073	0.00117	2094	51	1721	20	1432	19	1381	22	20	2094	51
G30	0.11403	0.00196	4.98778	0.09723	0.3172	0.00486	0.08846	0.0063	1865	32	1817	16	1776	24	1713	117	2	1865	32
G28	0.11183	0.00153	4.91136	0.07885	0.31856	0.00442	0.08774	0.00507	1829	25	1804	14	1783	22	1700	94	1	1829	25
G26	0.12166	0.00203	5.72385	0.10889	0.34113	0.00514	0.08601	0.00665	1981	30	1935	16	1892	25	1668	124	2	1981	30
G13	0.17652	0.00234	10.13825	0.16225	0.41661	0.00596	0.1168	0.00667	2620	23	2447	15	2245	27	2233	121	9	2620	23

average fission track length for these samples ranges from  $13.5 \pm 1.4 \mu\text{m}$  to  $14.0 \pm 1.1 \mu\text{m}$ .

#### Zircon U-Pb age

Given the proximity of the sampling locations and plutons, the samples of BG-A and BG-B show similar zircon U-Pb ages. The results are provided in Tables 2 and 3. According to the zircon U-Pb age concordance diagram and weighted average age diagram (Fig. 2), the weighted average age of sample BG-B is  $134.6 \pm 2.5 \text{ Ma}$ , and that of sample BG-C is  $136.6 \pm 1.6 \text{ Ma}$ . These results indicate that the samples were crystallized in the Early Cretaceous.

#### Zircon (U-Th)/He

Five zircon grains from sample BG-A, and three zircon grains from samples BG-B and BG-C, respectively, were analyzed for ZHe. The results are listed in Table 4. The uncorrected single zircon (U-Th)/He ages range from 44.9 to 66.2 Ma. After  $\alpha$ -particle correction (Farley *et al.*,

1996), the weighted average ages for the single zircon grains are 84.6 Ma (BG-A), 78.1 Ma (BG-B), and 90.0 Ma (BG-C).

#### Apatite (U-Th)/He

Four apatite grains from sample BG-A, three grains from sample BG-B, and two grains from sample BG-C were analyzed for AHe. The apatite (U-Th)/He ages and Th/U ratios are listed in Table 5. The uncorrected single-grain apatite (U-Th)/He ages range from 40.6 to 95.9 Ma. After  $\alpha$ -particle correction (Farley *et al.*, 1996), the weighted average ages for the single apatite grains are 63.0 Ma (BG-A), 77.4 Ma (BG-B), and 82.8 Ma (BG-C).

#### Thermal history modelling: Modelling strategy

The thermal history modelling of a single sample was performed using the HeFty software (Ketchum, 2005) using the ZHe, AHe, and AFT age data of a single sample. The geological conditions used for thermal history simulation in this study are as follows: 1) the

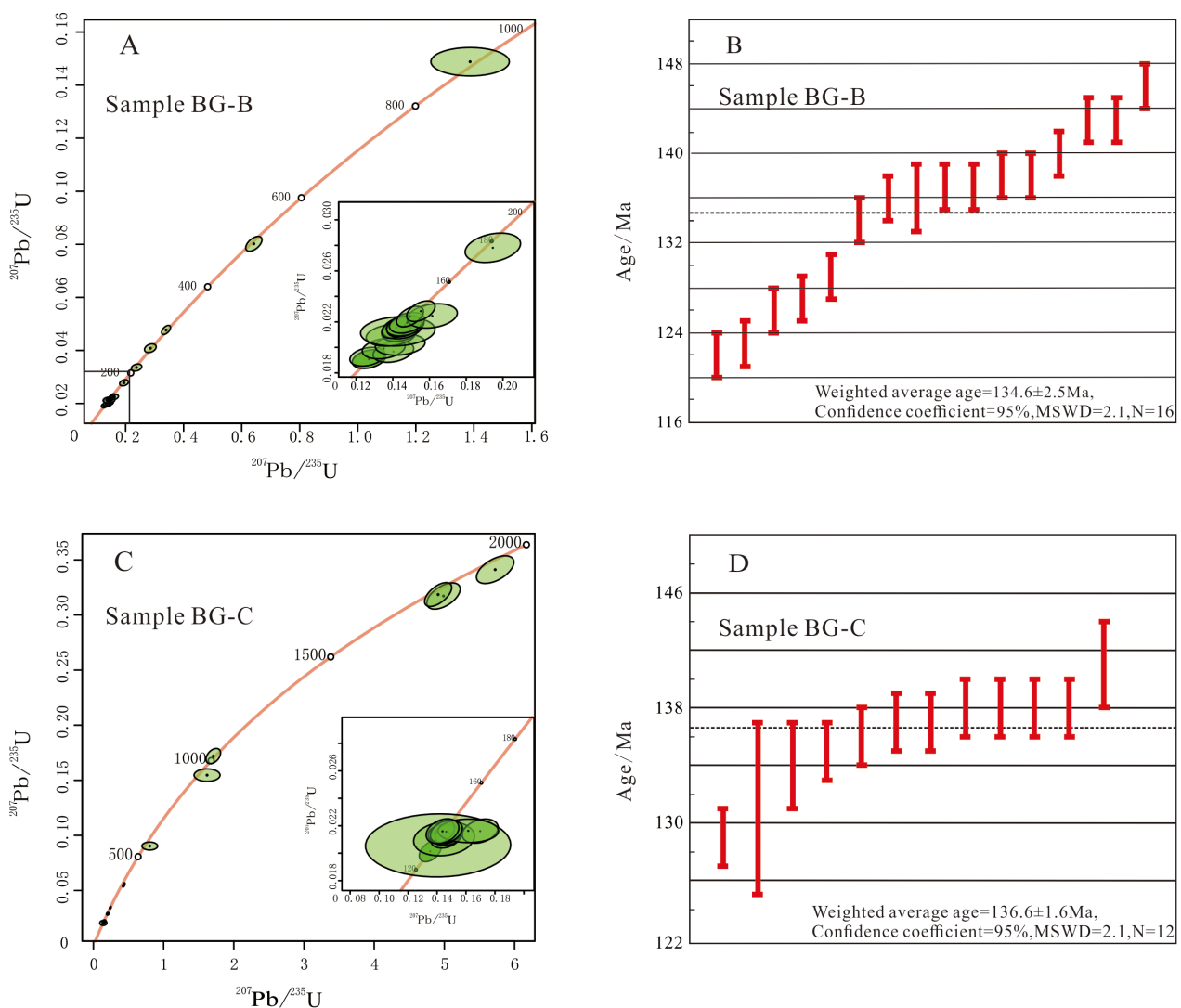


**FIGURE 2.** Samples of BG-B and BG-C zircon U-Pb age concordance diagrams (A, C) and weighted mean ages (B, D).

**TABLE 4.** Zircon (U-Th)/He analytical results of the Bange pluton in the Lhasa terrane.

Sample code	<sup>4</sup> He (ng)	± (%)	<sup>232</sup> Th (ng)	± (%)	<sup>238</sup> U (ng)	± (%)	Th/U	Ejection correction (%)	Raw age (Ma)	Ft-corrected age (Ma)	±1σ (Ma)	
BG-A												
G01	13.359	0.196	0.54	0.007	1.529	0.02	0.35	0.71	66.2	92.8	0.9	
G02	10.274	0.151	0.369	0.005	1.294	0.017	0.29	0.7	61.1	87.5	0.9	
G03	7.698	0.113	0.281	0.004	1.014	0.014	0.28	0.68	58.7	86.9	1	
G04	15.703	0.241	0.429	0.006	2.486	0.031	0.17	0.66	49.9	75.2	0.8	
G05	17.163	0.257	0.565	0.008	2.584	0.032	0.22	0.65	51.9	80.4	0.9	
									Weighted mean age (Ma)		84.6	0.9
BG-B												
G01	20.548	0.311	0.506	0.007	3.123	0.039	0.16	0.7	52	74.5	0.8	
G02	4.501	0.07	0.209	0.003	0.657	0.008	0.32	0.58	52.9	91.3	1	
G03	5.261	0.081	0.553	0.008	0.839	0.011	0.66	0.66	44.9	68.5	0.7	
									Weighted mean age (Ma)		78.1	0.84
BG-C												
G01	15.028	0.232	0.355	0.005	1.931	0.024	0.18	0.66	61.3	92.5	1	
G02	23.51	0.346	0.386	0.005	2.871	0.043	0.13	0.71	65	91.5	1.2	
G03	29.11	0.428	0.421	0.006	3.838	0.057	0.11	0.7	60.6	86.1	1.2	
									Weighted mean age (Ma)		90	1.13
FCT16-11	6.281	0.097	2.182	0.030	2.257	0.028	0.970	0.750	18.700	24.8	0.2	
FCT16-12	5.072	0.078	1.434	0.020	1.999	0.025	0.720	0.720	17.900	24.7	0.2	
FCT16-15	14.552	0.221	3.422	0.047	5.891	0.074	0.580	0.700	17.900	25.4	0.2	

**TABLE 5.** Apatite (U-Th)/He analytical results of the Bange pluton in the Lhasa terrane.

Sample code	<sup>4</sup> He (ng)	± (%)	<sup>232</sup> Th (ng)	± (%)	<sup>238</sup> U (ng)	± (%)	Th/U	Ejection correction (%)	Raw age (Ma)	Ft-corrected age (Ma)	±1σ (Ma)	
BG-A												
G01	0.925	0.141	0.024	0.000	0.127	0.013	0.19	0.76	57.1	74.9	6.6	
G02	0.308	0.050	0.012	0.000	0.075	0.027	0.15	0.69	32.6	47.3	15.7	
G03	0.503	0.086	0.018	0.000	0.140	0.024	0.13	0.71	28.7	40.6	6.3	
									Weighed mean age (Ma)		63.0	9.2
BG-B												
G01	1.555	0.021	0.254	0.003	0.198	0.003	1.28	0.74	49.5	66.5	0.7	
G02	1.071	0.015	0.037	0.001	0.141	0.007	0.27	0.67	58.8	88.2	3.5	
G03	1.520	0.021	0.021	0.000	0.169	0.015	0.12	0.75	71.7	95.9	7.6	
									Weighed mean age (Ma)		77.4	4.3
BG-C												
G01	1.613	0.022	0.026	0.000	0.197	0.015	0.13	0.77	65.0	84.8	5.8	
G02	0.681	0.009	0.020	0.000	0.098	0.013	0.20	0.67	54.4	80.7	9.5	
									Weighed mean age (Ma)		82.8	7.6
DUR1	7.891	2.061	6.741	0.079	0.286	0.004	23.530	1.000	34.600	34.6	0.4	
DUR2	8.493	2.304	7.070	0.082	0.085	0.001	83.430	1.000	39.800	39.8	0.5	
DUR3	8.397	2.361	7.412	0.087	0.286	0.003	25.950	1.000	33.900	33.9	0.4	
DUR4	5.717	1.664	5.054	0.059	0.209	0.003	24.140	1.000	33.500	33.5	0.4	
DUR5	8.359	2.517	7.740	0.091	0.274	0.004	28.220	1.000	32.700	32.7	0.4	

current surface temperature is  $10 \pm 10$  °C; 2) the initial time-temperature is limited to 220–170 °C initial time-temperature range of the cooling path is limited to 230–120 °C ZHe and AFT ages and 80–40 °C AHe ages. These pre-modelling settings have great uncertainty, which enables the modelling to search for a wide range of data-constrained thermal history as much as possible (Sun *et al.*, 2024).

#### *Results of thermal history modelling*

This study performed thermal history simulations on the ZHe, AHe, and AFT data obtained from three samples (BG-A, BG-B, and BG-C) (Fig. 3). The results indicate that sample BG-A cooled most rapidly between 94–72 Ma, at a rate of 2.36 °C/Ma; then, from 72–56 Ma, the cooling rate decreased to 0.22 °C/Ma; after 56 Ma, the cooling rate increased to 1.52 °C/Ma. Samples BG-B and BG-C exhibited similar cooling patterns to BG-A, with the fastest cooling occurring between 94–80 Ma at a rate of ~6.6 °C/Ma. Subsequently, the cooling rate gradually slowed to ~1.0 °C/Ma. Collectively, the thermal modelling shows that the Bange pluton underwent a rapid cooling (in average of ~4.2 °C/Ma) process in the Late Cretaceous, with a significant decrease in the cooling rate (~1.1 °C/Ma of average) in the Paleocene.

## **Discussion**

#### *The Late Cretaceous cooling history of the Bange pluton and tectonic uplift on the northern Lhasa*

The obtained low-temperature thermochronologic data show that the zircon and apatite (U-Th)/He ages, and apatite fission track ages of the samples from the Bange plutons are concentrated between 94 and 65 Ma. Based on the results of thermal history modelling, the three samples of the Bange pluton exhibit similar thermal histories in the Late Cretaceous period, experiencing rapid cooling during 94–70 Ma (Fig. 4). The former thermochronological thermal history modelling for the Bange plutons yielded that the rapid cooling occurred in the late Cretaceous to early Eocene (70–55 Ma) and followed by the slow cooling rate (Hetzl *et al.*, 2011; Haider *et al.*, 2013). In comparison, the rapid cooling time obtained in this study is a bit older, showing the age of ~94–70 Ma. The reason for this rapid cooling should be in further discussion. The Bange pluton, located in the Bangong-Nujiang suture zone, is closely linked to the closure of the Bangong-Nujiang Ocean and the collision and amalgamation of the Lhasa-Qiangtang terrane (Royden *et al.*, 2008; Rohrmann *et al.*, 2012). The magmatic gap in the Late Jurassic-early Early Cretaceous and the sedimentary records of the Shamuluo Formation marked the end of the subduction of

the Bangong-Nujiang Ocean, and the subsequent collision between the Lhasa and Qiangtang terranes (Hu *et al.*, 2022). The sedimentary environment and provenance of Lower-Middle Cretaceous sequences (*i.e.*, the Duoni Formation) in the Bange area, suggest that the Bangong-Nujiang suture zone have been closed before the Early Cretaceous (~114 Ma), in response to the collision of the Lhasa and Qiangtang terranes (Zhu *et al.*, 2020). Such sedimentary record is also observed in the west part of the Bangong-Nujiang belt (Kapp *et al.*, 2007). Tectonic restoration shows that the Lhasa terrane was significantly affected by the closure of the Bangong-Nujiang Ocean, with ~50% of the crustal shortening and thickening occurring between 100 and 50 Ma (Murphy *et al.*, 1997; Kapp *et al.*, 2005, 2007; Li *et al.*, 2015). Therefore, thermochronological data from the Bange area indicate rapid cooling in the Late Cretaceous, with a cooling rate of about 4.2 °C/Ma, which significantly slowed to about 1.1 °C/Ma since 65 Ma. This rapid cooling event may be related to the regional crustal shortening and thickening caused by the collision of the Lhasa and Qiangtang terranes.

Extensive thermochronological data from the Bangong-Nujiang suture zone (*e.g.*, Coqin, Gaize, Nima) show ZHe ages of ~110–67 Ma, AFT ages of ~61–45 Ma, and AHe ages of ~63–40 Ma (Sun *et al.*, 2024). Sun *et al.* (2024) conducted low-temperature thermochronological research on rock samples from the Coqin Basin, concluding that the Coqin Basin in northern Lhasa rapidly cooled and uplifted at ~80–40 Ma. Li *et al.* (2022) identified the multi-stage cooling process of the Gaize Basin using methods such as (U-Th)/He and fission track of detrital zircon and apatite, showing a rapid cooling history in the Late Cretaceous-Paleocene period similar to this study. The Nima and Lunpola basins experienced uplift and the establishment of endorheic drainage systems in the Late Cretaceous to Early Oligocene (Han *et al.*, 2019; Xue *et al.*, 2022). The southern part of the Qiangtang Terrane has multi-stage cooling history, with ZHe ages between ~150–80 Ma, AFT ages between ~95–44 Ma, and AHe ages between ~85–40 Ma (Zhao *et al.*, 2017; Yang *et al.*, 2019; Qian *et al.*, 2021; Xue *et al.*, 2022). Based on the regional published data and this study, rapid cooling occurred synchronously in the whole northern Lhasa area of the central Tibetan Plateau during the Late Cretaceous-Paleocene (94–65 Ma). Comprehensive regional low-temperature thermochronological data and thermal history show that the central Tibetan Plateau (northern Lhasa terrane, Bangong-Nujiang suture zone, and southern Qiangtang terrane) experienced rapid cooling between 94 and 65 Ma, with the cooling rate slowing significantly between ~65 and 40 Ma (Hetzl *et al.*, 2011; Rohrmann *et al.*, 2012; Haider *et al.*, 2013; Li *et al.*, 2022; Sun *et al.*, 2024) (Fig. 3). This synchronous uplift process indicates a relatively consistent uplift period in the Late Cretaceous.

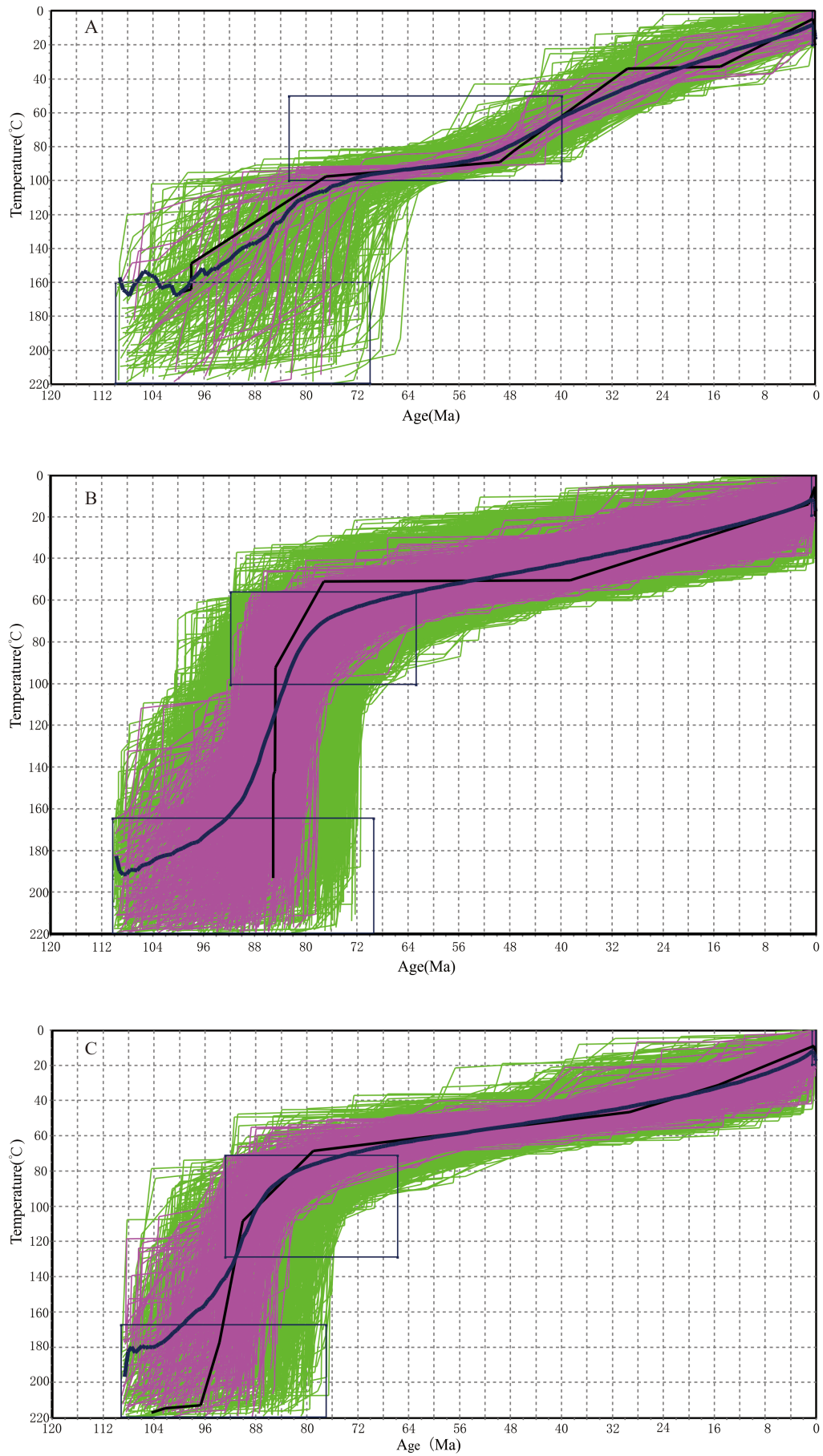


**FIGURE 3.** Thermal history modelling by the HeFTy of sample BG-A (A), sample BG-B (B) and sample BG-C (C).

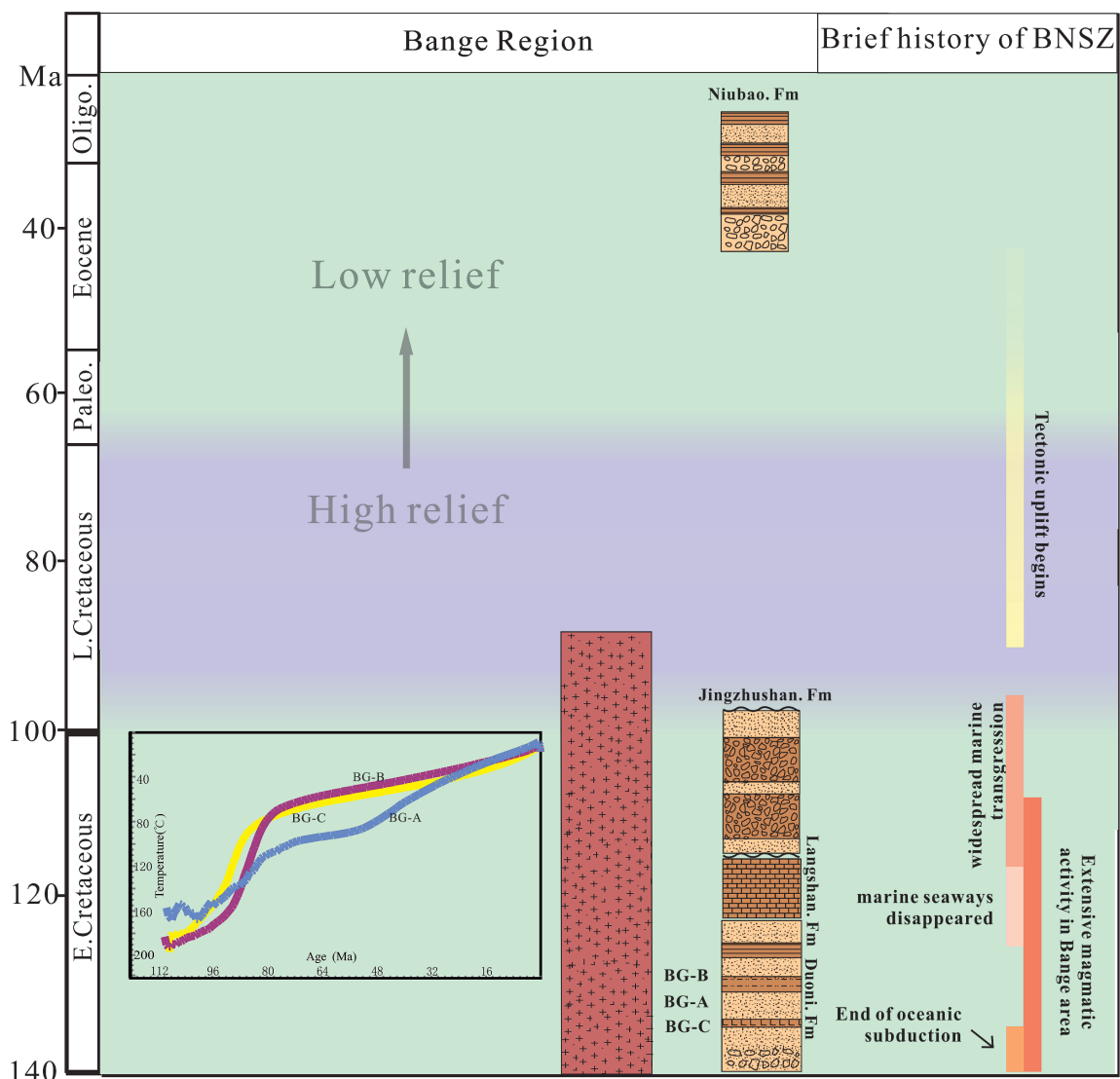


**FIGURE 4.** The Late Cretaceous rapid cooling history of the Bange pluton and a brief evolutionary history of the BNSZ. Sources from Sun, 2015a, 2024; Hu *et al.*, 2022.

Significant magmatic activity in the Bangong-Nujiang suture zone and adjacent areas developed between ~130–90 Ma, with post-collision residual marine sediments widely present (Zhang *et al.*, 2012, 2014; Sun, 2015; Lai *et al.*, 2019). The activity of potassium-rich magma and adakitic or high-magnesium magma from 90 to 75 Ma indicates substantial crustal thickening and delamination in the Late Cretaceous (Li *et al.*, 2013; Wang *et al.*, 2014; Sun *et al.*, 2015a). These magmatic records document the crustal thickening under the Bangong-Nujiang suture zone during the Late Cretaceous. Structural deformation studies found that fold-thrust deformation and crustal shortening and thickening in the central Tibet Plateau during the Late Cretaceous were primarily north-south, including the Coqin fold-thrust belt (>50 Ma), Gaize-Selin Co thrust belt (99–23 Ma), and Shiquanhe-Gaize-Anduo thrust belt (116–23 Ma) from south to north (Li *et al.*, 2015).

Most of these thrust belts developed before the India-Asia continent collision (~60–50 Ma) (Li *et al.*, 2015). Based on the tectonic background and research in central Tibet, significant shortening and thickening of the Lhasa terrane crust before the India-Asia collision are attributed to the collision between the Lhasa and Qiangtang terranes (Hinsbergen *et al.*, 2011).

The Late Cretaceous tectonic uplift is also reflected in the sedimentary record. In the North Lhasa terrane, after the deposition of marine Langshan Formation limestone in the Late Cretaceous (~90 Ma) (Sun *et al.*, 2017; Xu *et al.*, 2022), two sets of continental molasse deposits were rapidly uplifted and developed: the Daxiong Formation alluvial fan conglomerates in the south; and the Jingzhushan Formation in the north (Kapp *et al.*, 2007; Sun *et al.*, 2015a; Lai *et al.*, 2019). The region experienced a sedimentary hiatus until ~60–50 Ma when

continental fluvial-lake deposits developed again. This marine-continental sedimentary transition at ~90 Ma and the subsequent ~30–40 Ma depositional hiatus are likely controlled by regional tectonic uplift, as indicated by the rapid cooling history of the Late Cretaceous observed in this study. This transition from a marine to continental environment, followed by rapid uplift and erosion has occurred all over the Northern Lhasa subterrane (Sun *et al.*, 2015a; Lai *et al.*, 2019). Combined with the above geological background, we suggest that the synchronous cooling process in the central Tibetan Plateau in the Late Cretaceous was probably driven by the collision of the Lhasa-Qiangtang terrane and subsequent large-scale crustal shortening and thickening. This process resulted in crustal thickening through thrust faults, leading to significant tectonic uplift (Fig. 4) (Sun *et al.*, 2015a; Lai *et al.*, 2019).

#### *Implications for the geomorphologic evolution of the central Tibetan Plateau*

The present-day topography of the central Tibetan Plateau is characterized by high altitude (approximately 5000 meters on average) and low-relief landscape (Han *et al.*, 2019). Such low-relief topography generally exhibits low denudation rates (Lal *et al.*, 2004; Sun *et al.*, 2024). The rapid uplift of the Lhasa terrane in the Late Cretaceous inevitably accompanied denudation processes. During the Late Cretaceous (approximately 88–83 Ma), the sources of turbidites in the Xigaze forearc basin were primarily from the Gangdese arc and the Northern Lhasa terrane (An *et al.*, 2014). Based on the sediment source transport characteristics and the rapid cooling history of the Lhasa terrane during the Late Cretaceous, it is suggested that the Tibetan Plateau may have featured high-elevation and high-relief geomorphology before the India-Asia continental collision. Compared to the Late Cretaceous cooling rate, the lower cooling rate after 65 Ma (~1.1 °C/Ma) may be associated with the gradual smoothening of the Lhasa terrane topography.

At approximately 90 Ma, the terrestrial Daxiong Formation and Jingzhushan Formation molasses sediment source in the northern Lhasa terrane was primarily derived from the uplifted northern Lhasa terrane denudation (Sun *et al.*, 2015a). Subsequently, the Lhasa terrane entered a sedimentary hiatus (Sun *et al.*, 2024), indicating that the northern Lhasa terrane acted as a sediment source area, transporting sediment externally. This suggests the development of a large-scale external sediment transport channel in the Lhasa terrane at that time. Current research from the Lunpola Basin in the central Tibetan Plateau reveal the existence of a “central valley” with low elevation in the Bangong-Nujiang suture zone around 50–40 Ma (Fang *et al.*, 2020; Xiong *et al.*, 2022). This central valley may have been formed by the Late

Cretaceous orogenic collapse and the early uplift of the Eocene Qiangtang terrane and the southern Lhasa terrane (Hu *et al.*, 2020). Consequently, it is plausible that a Late Cretaceous–Paleocene external sedimentary transport system developed in the central valley. Although there is no definitive study on the restoration of this external palaeohydrological system. Geological evidence from the Lhasa terrane suggests that during the Late Cretaceous, detrital materials in the northern Lhasa terrane were transported southward via the Palaeo-Lhasa River and ultimately deposited into the Trench Basin (Orme *et al.*, 2015; Laskowski *et al.*, 2019).

In the study of river system evolution and provenance since the Eocene–Oligocene, no sediment information from the central Qiangtang uplift, the Anduo microterrane, etc. was found, which may suggest that the river network in central Tibet no longer drained water in the Eocene. (Metcalf & Kapp 2017; Han *et al.*, 2019; Xue *et al.*, 2022). Miocene lakes in the Lunpola and Nima basins in central Tibet transitioned to a hypersaline state (Wang *et al.*, 2011a, b). This, combined with the paleocurrent direction, suggests that central Tibet has been hydrologically closed since the Eocene (Han *et al.*, 2019; Xue *et al.*, 2022). The development of an internal flow system is crucial for forming low-relief topography through sediment redistribution (Liu *et al.*, 2008). Coupled with the low cooling rate since the Eocene, this indicates that low-relief topography and endorheic systems have developed in central Tibet since at least the Eocene.

## **Conclusion**

According to zircon U–Pb and low-temperature thermochronology data from samples obtained in the Bange area, the thermal history model indicates that the Bange area experienced a rapid cooling stage in the Late Cretaceous (94–70 Ma). Based on regional data comparison and geological background, it is believed that the collision between the Lhasa terrane and the Qiangtang terrane caused the uplift of the Lhasa terrane in the Late Cretaceous. Coupled with provenance analysis and the lower cooling rate since the Eocene, this suggests that low-relief terrain has been developed in central Tibet since at least the Eocene.

## **Acknowledgments**

We sincerely thank Finlay Stuart, Cristina Persano, Katarzyna Luszczak and Luigia Di Nicola for their help on the AFT, ZHe and AHe analyses in thermochronology laboratories of University of Glasgow and Scottish

Universities Environmental Research Centre. This study was financially supported by the National Key R & D Program of China (2022YFF0800800), the National Natural Science Foundation of China (Grant No. 42072124), and the Second Tibetan Plateau Scientific Expedition and Research Program (STEP, Grant No. 2019QZKK0204).

## References

- An, W., Hu, X.M., Garzanti, E., BouDagher-Fadel, M.K., Wang, J.G. & Sun, G.Y. (2014) Xigaze forearc basin revisited (South Tibet): Provenance changes and origin of the Xigaze Ophiolite. *Geological Society of America Bulletin*, 126 (11–12), 1595–1613.  
<https://doi.org/10.1130/B31020.1>
- Bi, W.J., Han, Z.P., Li, Y.L., Li, C.M., Wang, C.S., Zhang, J.W., Han, J.Y., He, H.Y., Qian, X.Y., Xu, T.K. & Ma, Z.N. (2021) Deformation and cooling history of the Central Qiangtang terrane, Tibetan Plateau and its tectonic implications. *International Geology Review*, 63 (15), 1821–1837.  
<https://doi.org/10.1080/00206814.2020.1795733>
- Dai, J.G., Wang, C.S., Hourigan, J. & Santosh, M. (2013) Insights into the early Tibetan Plateau from (U-Th)/He thermochronology. *Journal of the Geological Society*, 170 (6), 917–927.  
<https://doi.org/10.1144/jgs2012-076>
- Dai, J.G., Fox, M., Shuster, D.L., Hourigan, J., Han, X., Li, Y.L. & Wang, C.S. (2020) Burial and exhumation of the Hoh Xil Basin, northern Tibetan Plateau: Constraints from detrital (U-Th)/He ages. *Basin Research*, 32 (5), 894–915.  
<https://doi.org/10.1111/bre.12405>
- Ding, L. & Lai, Q.Z. (2003) New geological evidence of crustal thickening in the Gangdese block prior to the Indo-Asian collision. *Chinese Science Bulletin*, 49, 1604–1610.  
<https://doi.org/10.1007/BF03183969>
- Ding, L., Kapp P., Cai F., Garzanti C.N., Xiong Z., Wang H. & Wang C. (2022) Timing and mechanisms of Tibetan Plateau uplift. *Nature Reviews earth & environment*, 3, 652–667.  
<https://doi.org/10.1038/s43017-022-00318-4>
- Farley, K.A., Wolf, R.A. & Silver, L.T. (1996) The effects of long alpha-stopping distances on (U-Th)/He ages. *Geochimica Et Cosmochimica Acta*, 60 (21), 4223–4229.  
[https://doi.org/10.1016/S0016-7037\(96\)00193-7](https://doi.org/10.1016/S0016-7037(96)00193-7)
- Fang, X.M., Dupont-nivet, G., Wang, C.S., Song, C.H., Meng, Q.Q., Zhang, W.L., Nie, J.S., Zhang, T., Mao, Z.Q. & Chen, Y. (2020) Revised chronology of central Tibet uplift (Lunpola Basin). *Science Advances*, 6 (50), eaba7298.  
<https://doi.org/10.1126/sciadv.aba7298>
- Haider, V.L., Dunkl, I., Eynatten, H., Ding, L., Frei, D. & Zhang, L.Y. (2013) Cretaceous to Cenozoic evolution of the northern Lhasa Terrane and the Early Paleogene development of peneplains at Nam Co, Tibetan Plateau. *Journal of Asian Earth Sciences*, 70–71, 79–98.  
<https://doi.org/10.1016/j.jseas.2013.03.005>
- Han, Z.P., Sinclair, H.D., Li, Y.L., Wang, C.S., Tao, Z., Qian, X.Y., Ning, Z.J., Zhang, J.W., Wen, Y.X., Lin, J., Zhang, B.S., Xu, M., Dai, J.G., Zhou, A., Liang, H.M. & Cao, S. (2019) Internal drainage has sustained low-relief Tibetan Landscapes Since the early Miocene. *Geophysical Research Letters*, 46 (15), 8741–8752.  
<https://doi.org/10.1029/2019GL083019>
- He, S.L., Ding, L., Xiong, Z.Y., Spicer, R.A., Farnsworth, A., Valdes, P.J., Wang, C., Cai, F.L., Wang, H.Q., Sun, Y., Zeng, D., Xie, J., Yue, Y.H., Zhao, C.Y., Song, P.P. & Wu, C. (2022) A distinctive Eocene Asian monsoon and modern biodiversity resulted from the rise of eastern Tibet. *Science Bulletin*, 67 (21), 2245–2258.  
<https://doi.org/10.1016/j.scib.2022.10.006>
- Hetzl, R., Dunkl, I., Haider, V., Strobl, M., Eynatten, H., Ding, L. & Frei, D. (2011) Peneplain formation in southern Tibet predates the India-Asia collision and plateau uplift. *Geology*, 39 (10), 983–986.  
<https://doi.org/10.1130/G32069.1>
- Hetzl, R. (2013) Active faulting, mountain growth, and erosion at the margins of the Tibetan Plateau constrained by in situ-produced cosmogenic nuclides. *Tectonophysics*, 582 (2013), 1–24.  
<https://doi.org/10.1016/j.tecto.2012.10.027>
- Hinsbergen, D.J., Steinberger, B., Doubrovine, P.V. & Gassmüller, R. (2011) Acceleration and deceleration of India-Asia convergence since the Cretaceous: Roles of mantle plumes and continental collision. *Journal of Geophysical Research-Solid Earth*, 116 (B6).  
<https://doi.org/10.1029/2010JB008051>
- Hu, D.G., Wu, Z.H., Jiang, W., Shi, Y., Ye, P.S. & Liu, Q.S. (2005) SHRIMP zircon U-Pb age and Nd isotopic study on the Nyainqêntanglha Group in Tibet. *Science in China Series D: Earth Sciences*, 48 (9), 1377–1386.  
<https://doi.org/10.1360/04yd0183>
- Hu, F.Y., Wu, F.Y., Chapman, J.B., Ducea, M.N., Ji, W.Q. & Liu, S.W. (2020) Quantitatively tracking the elevation of the Tibetan Plateau since the Cretaceous: Insights from whole-rock Sr/Y and La/Yb ratios. *Geophysical Research Letters*, 47 (15).  
<https://doi.org/10.1029/2020GL089202>
- Hu, X.M., Ma, A.L., Xue, W.W., Garzanti, E., Cao, Y., Li, S.M., Sun, G.Y. & Lai, W. (2022) Exploring a lost ocean in the Tibetan Plateau: Birth, growth, and demise of the Bangong-Nujiang Ocean. *Earth-Science Reviews*, 229, 104031.  
<https://doi.org/10.1016/j.earscirev.2022.104031>
- Jackson, S.E., Pearson, N.J., Griffin, W.L. & Belousova, E.A. (2004) The application of laser ablation-inductively coupled plasma-mass spectrometry to in situ U-Pb zircon geochronology. *Chemical Geology*, 211 (1–2), 47–69.  
<https://doi.org/10.1016/j.chemgeo.2004.06.017>
- Kapp, P., Yin, A., Harrison, T.M. & Ding, L. (2005) Cretaceous-Tertiary shortening, basin development and volcanism in

- central Tibet. *Geological Society of America Bulletin*, 117, 865–878.  
<https://doi.org/10.1130/B25595.1>
- Kapp, P., DeCelles, P.G., Gehrels, G.E., Heizler, M. & Lin, D. (2007) Geological records of the Lhasa-Qiangtang and Indo-Asian collisions in the Nima area of central Tibet. *GSA Bulletin*, 119 (7-8), 917–933.  
<https://doi.org/10.1130/B26033.1>
- Kapp, P. & Decelles, P.G. (2019) Mesozoic-Cenozoic geological evolution of The Himalayan-Tibetan orogen and working tectonic Hypotheses. *American Journal of Science*, 319 (3), 159–254.  
<https://doi.org/10.2475/03.2019.01>
- Ketchum, R.A. (2005) Forward and inverse modelling of low-temperature thermochronometry data. *Reviews in Mineralogy and Geochemistry*, 58 (1), 275–314.  
<https://doi.org/10.2138/rmg.2005.58.11>
- Lai, W., Hu, X.M., Garzanti, E., Sun, G.Y., Garzzone, C.N., Fadel, M.B. & Ma, A.L. (2019) Initial growth of the Northern Lhasaplano, Tibetan Plateau in the early Late Cretaceous (ca. 92 Ma). *Geological Society of America Bulletin*, 131 (11-12), 1823–1836.  
<https://doi.org/10.1130/B35124.1>
- Lal, D., Harris, N.B.W., Sharma, K.K., Gu, Z.Y., Ding, L., Liu, T.S., Dong, W.Q., Caffee, M.W. & Jull, A.J.T. (2004) Erosion history of the Tibetan Plateau since the last interglacial: Constraints from the first studies of cosmogenic <sup>10</sup>Be from Tibetan bedrock. *Earth and Planetary Science Letters*, 217 (1-2), 33–42.  
[https://doi.org/10.1016/S0012-821X\(03\)00600-9](https://doi.org/10.1016/S0012-821X(03)00600-9)
- Laskowski, A.K., Orme, D.A., Cai, F.L. & Ding, L. (2019) The Ancestral Lhasa River: A Late Cretaceous trans-arc river that drained the proto-Tibetan Plateau. *Geology*, 47 (11), 1029–1033.  
<https://doi.org/10.1130/G46823.1>
- Li, C., Zhao, Z.B., Lu, H.J. & Li, H.B. (2022) Late Mesozoic-Cenozoic multistage exhumation of the central Bangong-Nujiang Suture, Central Tibet. *Tectonophysics*, 827, 229268.  
<https://doi.org/10.1016/j.tecto.2022.229268>
- Li, G.W., Kohn, B., Sandiford, M., Ma, Z.L. & Xu, Z.Q. (2018) Post-collisional exhumation of the Indus-Yarlung suture zone and northern Tethyan Himalaya, Saga, SW Tibet. *Gondwana Research*, 64, 1–10.  
<https://doi.org/10.1016/j.gr.2018.06.006>
- Li, G.W., Kohn, B., Sandiford, M., Xu, Z.Q. & Wei, L.J. (2015) Constraining the age of Liuqu Conglomerate, southern Tibet: Implications for evolution of the India-Asia collision zone. *Earth and Planetary Science Letters*, 426, 259–266.  
<https://doi.org/10.1016/j.epsl.2015.06.010>
- Li, H.A., Dai, J.G., Xu, S.Y., Liu, B.R., Han, X., Wang, Y.N. & Wang, C.S. (2019) The formation and expansion of the eastern Proto-Tibetan Plateau: Insights from low-temperature thermochronology. *Journal of Asian Earth Sciences*, 183, 103975.  
<https://doi.org/10.1016/j.jseas.2019.103975>
- Li, Y.L., He, J., Wang, C.S., Santosh, M., Dai, J.G., Zhang, Y.X., Wei, Y.S. & Wang, J.G. (2013) Late Cretaceous K-rich magmatism in central Tibet: Evidence for early elevation of the Tibetan plateau? *Lithos*, 160-161, 1–13.  
<https://doi.org/10.1016/j.lithos.2012.11.019>
- Li, Y.L., Wang, C.S., Dai, J.G., Xu, G.Q., Hou, Y.L. & Li, X.H. (2015) Propagation of the deformation and growth of the Tibetan–Himalayan orogen: A review. *Earth-Science Reviews*, 143, 36–61.  
<https://doi.org/10.1016/j.earscirev.2015.01.001>
- Liu, Z., Tapponnier, P., Gaudemer, Y. & Ding, L. (2008) Quantifying landscape differences across the Tibetan plateau: Implications for topographic relief evolution. *Journal of Geophysical Research-Earth Surface*, 113 (F4).  
<https://doi.org/10.1029/2007JF000897>
- Lu, L., Zhao, Z., Wu, Z.H., Qian, C. & Ye, P.S. (2015) Fission track thermochronology evidence for the Cretaceous and Paleogene tectonic event of Nyainrong microcontinent, Tibet. *Acta Geologica Sinica-English Edition*, 89 (1), 133–144.  
<https://doi.org/10.1111/1755-6724.12400>
- Metcalfe, K. & Kapp, P. (2017) The Yarlung suture melange, Lopus Range, southern Tibet: Provenance of sandstone blocks and transition from oceanic subduction to continental collision. *Gondwana Research*, 48, 15–33.  
<https://doi.org/10.1016/j.gr.2017.03.002>
- Murphy, M.A., Yin, A., Harrison, T.M., Dürr, S.B., Chen, Z., Ryerson, F.J., Kidd, W.S.F., Wang, X. & Zhou, X. (1997) Did the Indo-Asian collision alone create the Tibetan plateau? *Geology*, 25 (8), 719–722.  
[https://doi.org/10.1130/0091-7613\(1997\)025<0719:DTIACA>2.3.CO;2](https://doi.org/10.1130/0091-7613(1997)025<0719:DTIACA>2.3.CO;2)
- Orme, D.A., Carrapa, B. & Kapp, P. (2015) Sedimentology, provenance and geochronology of the upper Cretaceous-lower Eocene western Xigaze forearc basin, southern Tibet. *Basin Research*, 27 (4), 387–411.  
<https://doi.org/10.1111/bre.12080>
- Pan, G.T., Mo, X.X., Hou, Z.Q., Zhu, D.C., Wang, L.Q., Li, G.M., Zhao, Z.D., Geng, Q.R. & Liao, Z.L. (2006) Spatial-temporal framework of the Gangdese Orogenic Belt and its evolution. *Acta Petrologica Sinica*, 22 (3), 521–533.
- Qian, X.Y., Li, Y.L., Dai, J.G., Wang, C.S., Han, Z.P., Zhang, J.W. & Li, H. (2021) Apatite and zircon (U-Th)/He thermochronological evidence for Mesozoic exhumation of the Central Tibetan Mountain Range. *Geological Journal*, 56 (1), 599–611.  
<https://doi.org/10.1002/gj.3979>
- Reiners, P.W. (2005) Zircon (U-Th)/He thermochronometry. *Reviews in Mineralogy and Geochemistry*, 58 (1), 151–179.  
<https://doi.org/10.2138/rmg.2005.58.6>
- Royden, L.H., Burchfiel, B.C. & Van Der Hilst, R.D. (2008) The Geological Evolution of the Tibetan Plateau. *Science*, 321, 1054–1058.  
<https://doi.org/10.1126/science.1155371>

- Rohrmann, A., Kapp, P., Carrapa, B., Reiners, P.W., Guynn, J., Ding, L. & Heizler, M. (2012) Thermochronologic evidence for plateau formation in central Tibet by 45 Ma. *Geology*, 40 (2), 187–190.  
<https://doi.org/10.1130/G32530.1>
- Shi, Y.F., Li, J.J., Li, B.Y., Yao, T.D., Wang, S.M., Li, S.J., Cui, Z.J., Wang, F.B., Pan, B.T., Fang, X.M. & Zhang, Q.S. (1999) Uplift of The Qinghai-Xizang (Tibetan) Plateau and East Asia environmental change during Late Cenozoic. *Acta Geographica Sinica*, 54 (1), 10–20.  
<https://doi.org/10.11821/xb199901002>
- Staisch, L.M., Niemi, N.A., Clark, M.K. & Chang, H. (2016) Eocene to late Oligocene history of crustal shortening within the Hoh Xil Basin and implications for the uplift history of the northern Tibetan Plateau. *Tectonics*, 35, 862–895.  
<https://doi.org/10.1002/2015TC003972>
- Strobl, M., Hetzel, R., Ding, L., Zhang, L.Y. & Hampel, A. (2010) Preservation of a large-scale bedrock peneplain suggests long-term landscape stability in southern Tibet. *Zeitschrift für Geomorphologie*, 54 (10), 453–466.  
<https://doi.org/10.1127/0372-8854/2010/0054-0023>
- Sun, G.Y., Hu, X.M., Sinclair, H.D., BouDagher-Fadel, M.K. & Wang, J.G. (2015a) Late Cretaceous evolution of the Coqen Basin (Lhasa terrane) and implications for early topographic growth on the Tibetan Plateau. *Geological Society of America Bulletin*, 127 (7-8), 1001–1020.  
<https://doi.org/10.1130/B31137.1>
- Sun, G.Y., Hu, X.M., Zhu, D.C., Hong, W.T., Wang, J.G. & Wang, Q. (2015b) Thickened juvenile lower crust-derived ~90Ma adakitic rocks in the central Lhasa terrane, Tibet. *Lithos*, 225–239.  
<https://doi.org/10.1016/j.lithos.2015.03.010>
- Sun, G.Y., Sinclair, H.D., Persano, C., Stuart, F.M. & Hu, X.M. (2024) Late Cretaceous-Eocene exhumation of the northern Lhasa terrane and topographic implications for the Central Tibet. *Lithos*, 470–471.  
<https://doi.org/10.1016/j.lithos.2024.107528>
- Sun, G.Y. (2015) *Sedimentary Evolution of the Cretaceous Coqen Basin (Southern Tibet) and Implications for Early Topographic Growth on the Lhasa Terrane*. PhD thesis, Nanjing University, Nanjing. 161 pp.
- Sun, G.Y., Hu, X.M. & Sinclair, H.D. (2017) Early Cretaceous palaeogeographic evolution of the Coqen Basin in the Lhasa Terrane, southern Tibetan Plateau. *Palaeogeography, Palaeoclimatology, Palaeoecology*, 485, 101–118.  
<https://doi.org/10.1016/j.palaeo.2017.06.006>
- Tong, K., Li, Z.W., Zhu, L.D., Xu, G.Q., Zhang, Y.X., Kamp, P.J., Tao, G., Yang, W.G., Li, J.X., Wang, Z.J., Jiang, X. & Zhang, H.S. (2022) Thermochronology constraints on the Cretaceous-Cenozoic thermo-tectonic evolution in the Gaize region, central-western Tibetan Plateau: Implications for the westward extension of the proto-Tibetan Plateau. *Journal of Asian Earth Sciences*, 240, 105419.  
<https://doi.org/10.1016/j.jseas.2022.105419>
- Wang, C.S., Dai, J.G., Zhao, X.X., Li, Y.L., Graham, S.A., He, D.F., Ran, B. & Meng, J. (2014) Outward-growth of the Tibetan Plateau during the Cenozoic: A review. *Tectonophysics*, 621, 1–43.  
<https://doi.org/10.1016/j.tecto.2014.01.036>
- Wang, L.C., Wang, C.S., Li, Y.L., Zhu, L.D. & Wei, Y.S. (2011a) Sedimentary and organic geochemical investigation of tertiary lacustrine oil shale in the central Tibetan plateau: Palaeolimnological and palaeoclimatic significances. *International Journal of Coal Geology*, 86 (2-3), 254–65.  
<https://doi.org/10.1016/j.coal.2011.02.011>
- Wang, L.C., Wang, C.S., Li, Y.L. & Zhu, L.D. (2011b) Organic geochemistry of potential source rocks in the Tertiary Dingqinghu Formation, Nima Basin, Central Tibet. *Journal of Petroleum Geology*, 34 (1), 67–85.  
<https://doi.org/10.1111/j.1747-5457.2011.00494.x>
- Wang, L.C. & Wei, Y.S. (2013) Apatite fission track thermochronology evidence for the Mid-Cretaceous tectonic event in the Qiangtang Basin, Tibet. *Acta Petrologica Sinica*, 29 (3), 1039–1047.
- Wang, Q., Zhu, D.C., Zhao, Z.D., Liu, S.A., Chung, S.L., Li, S.M., Liu, D., Dai, J.G., Wang, L.Q. & Mo, X.X. (2014) Origin of the ca. 90 Ma magnesia-rich volcanic rocks in SE Nyima, central Tibet: Products of lithospheric delamination beneath the Lhasa-Qiangtang collision zone. *Lithos*, 198-199, 24–37.  
<https://doi.org/10.1016/j.lithos.2014.03.019>
- Wang, Y., Zhang, X.M., Sun, L.X. & Wan, J.L. (2007) Cooling history and tectonic exhumation stages of the south-central Tibetan Plateau (China): Constrained by 40Ar/39Ar and apatite fission track thermochronology. *Journal of Asian Earth Sciences*, 29 (2), 266–282.  
<https://doi.org/10.1016/j.jseas.2005.11.001>
- Wu, F.Y., Huang, B.C., Ye, K. & Fang, A.M. (2008) Collapsed Himalayan–Tibetan orogen and the rising Tibetan Plateau. *Acta Petrologica Sinica*, 24 (1), 1–30.
- Xiong, Z.Y., Liu, X.H., Ding, L., Farnsworth, A., Spicer, R.A., Xu, Q., Valdes, P., He, S.L., Zeng, D., Wang, C., Li, Z.Y., Guo, X.D., Su, T., Zhao, C.Y., Wang, H.Q. & Yue, Y.H. (2022) The rise and demise of the Paleogene Central Tibetan Valley. *Science Advances*, 8 (6).  
<https://doi.org/10.1126/sciadv.abj0944>
- Xu, Y.W., Hu, X.M., Garzanti, E., BouDagher, F., Sun, G.Y., Lai, W. & Zhang, S.J. (2022) Mid-Cretaceous thick carbonate accumulation in Northern Lhasa (Tibet): eustatic vs. tectonic control? *GSA Bulletin*, 134 (1-2), 389–404.  
<https://doi.org/10.1130/B35930.1>
- Xue, W.W., Najman, Y., Hu, X.M., Persano, C., Stuart, F.M., Li, W., Ma, A.L. & Wang, Y. (2022) Late Cretaceous to Late Eocene Exhumation in the Nima Area, Central Tibet: Implications for Development of Low Relief Topography of the Tibetan Plateau. *Tectonics*, 41 (3), e2021TC006989.  
<https://doi.org/10.1029/2021TC006989>
- Yang, H.H., Song, Y., Dilles, J.H., Sousa, F., Danisik, M. & Yang, C. (2019) The thermal-tectonic history of the Duolong

- ore district: Evidence from apatite (U-Th)/He dating. *Acta Petrologica Sinica*, 35 (3), 867–878.  
<https://doi.org/10.18654/1000-0569/2019.03.15>
- Yang, H.H., Song, Y., Tang, J.X., Wang, Q., Gao, K. & Wei, S.G. (2020) Low temperature history of the Tiegelongnan Porphyry-Epithermal Cu (Au) deposit in the Duolong Ore District of northwest Tibet, China. *Resource Geology*, 70 (2), 111–124.  
<https://doi.org/10.1111/rge.12221>
- Zhang, B.C., Fan, J.J., Luo, A.B., Li, H., Shen, D. & Liu, H.Y. (2022) Zircon U-Pb age, petrogenesis and tectonic model of Miocene quartz monzonite in Zuoquoxiang area, Western Lhasa terrane. *Geological Bulletin of China*, 41 (8), 1358–1368.  
<https://doi.org/10.12097/j.issn.1671-2552.2022.08.004>
- Zhang, K.J., Xia, B., Zhang, Y.X., Liu, W.L., Zeng, L., Li, J.F. & Xu, L.F. (2014) Central Tibetan Meso-Tethyan oceanic plateau. *Lithos*, 278–288.  
<https://doi.org/10.1016/j.lithos.2014.09.004>
- Zhang, K.J., Zhang, Y.X., Tang, X.C. & Xia, B. (2012) Late Mesozoic tectonic evolution and growth of the Tibetan plateau prior to the Indo-Asian collision. *Earth-Science Reviews*, 114 (3-4), 236–249.  
<https://doi.org/10.1016/j.earscirev.2012.06.001>
- Zhao, Z.B., Bons, P.D., Stübner, K., Wang, G.H. & Ehlers, T.A. (2017) Early Cretaceous exhumation of the Qiangtang Terrane during collision with the Lhasa Terrane, Central Tibet. *Terra Nova*, 29 (6), 382–391.  
<https://doi.org/10.1111/ter.12298>
- Zhao, Z.B., Bons, P.D., Li, C., Wang, G.H., Ma, X.X. & Li, G.W. (2020) The Cretaceous crustal shortening and thickening of the South Qiangtang Terrane and implications for proto-Tibetan Plateau formation. *Gondwana Research*, 78, 141–155.  
<https://doi.org/10.1016/j.gr.2019.09.003>
- Zhu, D.C., Mo, X.X., Zhao, Z.D. & Niu, Y.L. (2009) Permian and Early Cretaceous tectonomagmatism in southern Tibet and Tethyan evolution: New perspective. *Earth Science Frontiers*, 16 (2), 1–20.
- Zhu, D.C., Zhao, Z.D., Niu, Y.L., Dilek, Y., Hou, Z.Q. & Mo, X.X. (2013) The origin and pre-Cenozoic evolution of the Tibetan Plateau. *Gondwana Research*, 23 (4), 1429–1454.  
<https://doi.org/10.1016/j.gr.2012.02.002>
- Zhu, D.C., Zhao, Z.D., Niu, Y.L., Mo, X.X., Chung, S.L., Hou, Z.Q., Wang, L.Q. & Wu, F.Y. (2011) The Lhasa Terrane: Record of a microcontinent and its histories of drift and growth. *Earth and Planetary Science Letters*, 301 (1-2), 241–255.  
<https://doi.org/10.1016/j.epsl.2010.11.005>
- Zhu, Z.C., Zhai, Q.G., Hu, P.Y., Tang, Y., Wang, H.T., Wang, W., Wu, H. & Huang, Z.Q. (2020) Timing of the Lhasa-Qiangtang Collision: Constraints from the sedimentary records of the Doni Formation from the middle segment of the Bangong-Nujiang suture zone. *Acta Sedimentologica Sinica*, 38 (4), 712–726.  
<http://dx.doi.org/10.14027/j.issn.1000-0550.2019.081>